


# Inverse design and experimental realization of plasma metamaterials

Jesse A. Rodríguez\* and Mark A. Cappelli

Department of Mechanical Engineering, Stanford University, Stanford, California 94305, USA

 (Received 27 July 2023; revised 14 September 2023; accepted 18 September 2023; published 6 October 2023)

We apply inverse-design methods to produce two-dimensional triangular-lattice plasma-metamaterial (PMM) devices, which are then constructed and demonstrated experimentally. Finite-difference frequency-domain simulations are used along with forward-mode automatic differentiation to optimize the plasma densities of each of the plasma elements in the PMM to perform beam steering and demultiplexing under transverse magnetic polarization. The optimal device parameters are then used to assign plasma-density values to elements that make up an experimental version of the device. Device performance is evaluated against both the simulated results and human-designed alternatives, showing the benefits and disadvantages of *in silico* inverse design and paving the way for future fully *in situ* optimization.

DOI: [10.1103/PhysRevApplied.20.044017](https://doi.org/10.1103/PhysRevApplied.20.044017)

## I. INTRODUCTION

The inverse-design technique is aptly named; it consists of the process of optimizing a device given an *a priori* set of performance metrics. In electromagnetically active systems, the technique becomes a type of constrained-optimization problem, with Maxwell's equations serving as the constraints. The performance metrics are encoded in an objective function that increases with favorable performance, e.g.,  $L_2$  inner products of the electromagnetic (EM) field solutions for the current design iteration and the desired EM fields in regions of interest. This objective is a function of user-defined parameters that encode the domain and/or configuration of the device. This technique has been very fruitfully applied in EM systems over the past decade, leading to novel devices that perform functions so complex and at such high efficiencies that they would be impossible to realize through expert-level human design [1–7]. Some examples of such devices are high-performance metalenses [8,9], metasurfaces [10,11], photonic crystals [12–16], and even optical-computing devices that can perform functions such as Boolean-logic operations [17] and matrix-vector multiplication [18].

As mentioned above, in order to construct an objective that enables optimization of the device domain, the designer must come up with a parametrization scheme. Unfortunately, the configuration space of physically realizable devices is much smaller than the configuration space of devices that can be modeled, so the domain is parametrized in a manner that is in agreement with experimental facilities. Typically, given the limits of working with existing dielectric materials that have a fixed

dielectric response, the domain is binarized and the parameters simply correspond to whether or not material with a given dielectric constant is present at a location in the domain [19,20]. Of course, this limits the space of possible devices but nevertheless this approach has yielded startlingly strong results. There is also some exciting recent work that involves the use of additive manufacturing to produce two-dimensional (2D) devices with a finite number of gray-scale permittivity values within a certain interval through fine layering [21], greatly expanding the configuration space for inverse-design devices.

In this and previous studies [17,22], we choose to encode our device domain as a plasma metamaterial (PMM), i.e., as a domain filled with tunable plasma elements that can be reconfigured within a continuous range of permittivity values. A diagram that illustrates the inverse-design algorithm in our context is shown in Fig. 1. In a PMM, each of the device parameters corresponds to the plasma frequency (proportional to the square root of the plasma density) of one of the elements in the device. The plasma density is varied in practice by tuning the power delivery to the plasma elements; in our case, by increasing the power-supply voltage for a low-temperature gas discharge, but is possible by many methods in practice, such as tuning the power delivered to a resonator cavity or of the source of a laser-generated plasma. *In silico*, the domain is encoded as such and then a finite-difference frequency-domain simulation (FDFD) is computed using an autograd-compliant Maxwell solver called CEVICHE [23]. “Autograd-compliant” here means that by defining an objective that depends on the EM fields produced by the solver ( $L_2$  inner products as mentioned earlier), numerical gradients can easily be computed with respect to the parameters that encode the domain using a widely known PYTHON package. CEVICHE supplies the

\*jesse.rodriguez@oregonstate.edu

gradient of the fields with respect to the input parameters via forward-mode differentiation, a technique where the Jacobian is computed during the forward pass, e.g., as the solver progresses to produce the field solutions. The resulting gradient is then used to iteratively optimize the device.

The choice to encode the device as a PMM has a number of advantages that are a direct result of the unique dielectric response of the plasma. Figure 2 shows the way in which the dielectric permittivity of a nonmagnetized plasma varies with the incident wave frequency. The permittivity (neglecting the response of the ion) is of the following form, known as the Drude permittivity:

$$\varepsilon = 1 - \frac{\omega_p^2}{\omega^2 + i\omega\gamma},$$

where  $\gamma$  is the collision or damping rate,  $\omega_p^2 = n_e e^2 / \varepsilon_0 m_e$  is the plasma frequency squared,  $n_e$  is the electron density,  $e$  is the electron charge,  $m_e$  is the electron mass, and  $\varepsilon_0$  is the free-space permittivity. We can see from this functional

form that in the collisionless limit, the plasma permittivity can be tuned continuously in the interval  $(-\infty, 1)$  by varying the plasma density for a given operating frequency  $\omega$ . By choosing an operating frequency that is close to the plasma frequency of the elements, we can easily make drastic changes to their electromagnetic response; i.e., that of a metallic element or a near-zero-index medium. This dispersion relation not only makes the configuration space infinite as opposed to a binarized parametrization scheme but, much more importantly, this allows a single array of plasma elements to perform several functions, and since the plasma elements can be quickly deactivated, one can also switch the device on and off very quickly, in approximately 10 ms or less. More detail about switching times is given in Sec. II.

Most importantly, since all the parameters can be varied precisely in the physical device, it is possible to perform the inverse-design algorithm entirely *in situ*. This expedites the process of designing these devices by eliminating the need for expensive numerical simulations and also removes the errors associated with inaccurate modeling of the device elements. Fully *in situ* inverse design is just

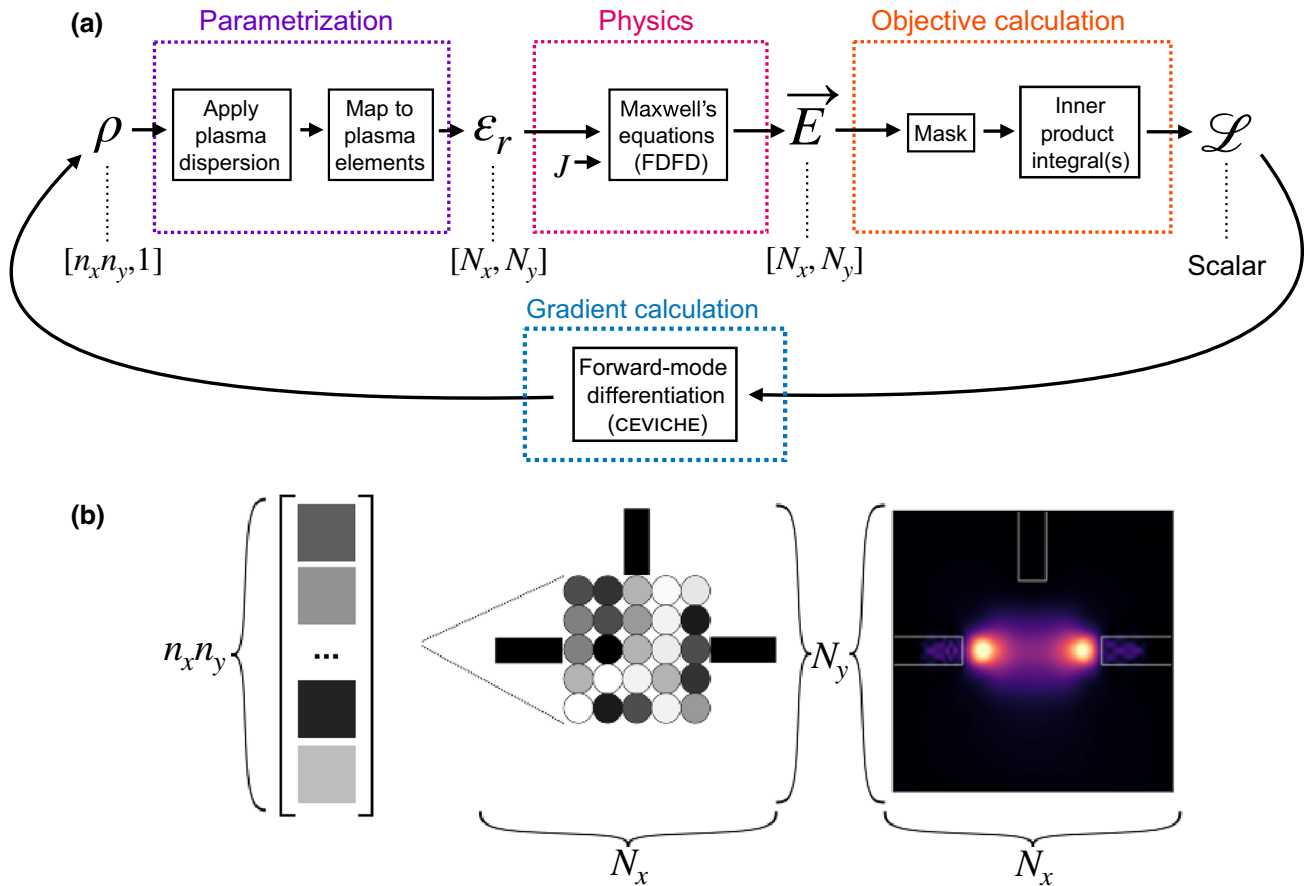


FIG. 1. (a) A flow chart describing the algorithmic design of our PMM array.  $J$  represents the modal source for the FDFD simulation. (b) Examples of the training parameter vector  $\rho$ , permittivity matrix  $\varepsilon_r$ , and simulated  $\vec{E}$  fields for a simple PMM device.

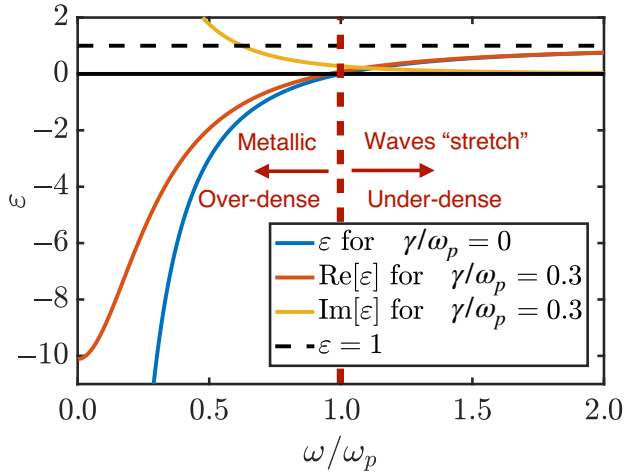


FIG. 2. The permittivity of nonmagnetized plasma versus the incident wave frequency normalized by the plasma frequency.

now becoming experimentally feasible [24] and the use of plasma in inverse-design devices offers high-precision continuous reconfigurability of device elements, attributes that are ideally suited for *in situ* optimization. In this study, we will examine the merits and disadvantages of creating inverse-design devices in the conventional way, by optimizing them *in silico* and then seeing how they perform experimentally. The development of the experimental platform that is detailed in this study will enable the transition to *in situ* inverse design in short order but first we must examine how our best *in silico* optimization efforts translate to experimental results. In the following sections, we will numerically optimize and experimentally demonstrate a 2D PMM that can perform both beam steering and demultiplexing.

## II. METHODS

### A. Computational inverse design

Figure 3(a) provides a diagram of our PMM device. The device has a triangular lattice with lattice spacing  $a = 24$  mm and is in the shape of a hexagon with six elements on each side, yielding 91 elements in total. The outer diameter of the  $\epsilon = 3.8$  quartz tubes is 15 mm and the inner diameter is 13 mm. In Fig. 3(b), the simulation domain is shown, with an arbitrary average plasma-density distribution among the elements, where each domain parameter corresponds to the space-averaged plasma frequency of one of the elements. The elements are modeled as either spatially uniform or as having a density profile that is axisymmetric and a zeroth-order Bessel function of the first kind of radius, with the first root at  $r = 6.5$  mm. In the collisional model (which is also nonuniform), the simulated elements have a collision frequency of  $\gamma = 1$  GHz. The blue line indicates where the source is located in

the domain and the red lines indicate the locations in the domain where the objective function is evaluated; we refer to these as “probe slices.” The probe slices surrounding the crystal are present to discourage leaking out of the device, while the probe slices within the exit horns either promote propagation into the correct horn or discourage propagation into the incorrect horn. The relative permittivity of the input and output horn walls was set to  $\epsilon = -1000$  to serve as a lossless metal and the horn geometry was chosen to match our experimental microwave horns (A INFO LB-20180 2–18 GHz).

The basic idea is that a modal source is introduced at the input horn and allowed to scatter through the training region before collecting at the desired output horn. In the computational-optimization phase, the fields are propagated through the domain via CEVICHE. As mentioned earlier, CEVICHE solves Maxwell’s equations using a FDFD solver and therefore all computed devices described here represent the steady-state solution achieved after some characteristic time. The simulation domain was discretized using a resolution of 50 pixels per lattice constant  $a$  and in each case presented dimensions of  $N_x = 1000$  and  $N_y = 1200$  pixels. The final device configurations were tested at the higher resolution of 150 pixels/ $a$  and yielded results that were qualitatively identical. A perfectly matched boundary layer (PML)  $2a$  in width was applied along the domain boundaries. The simulated  $\mathbf{E}$  fields were masked to compute integrals along the probe slices within the problem geometry. These integrals were used to calculate the objective  $\mathcal{L}(\rho)$ . Our simulation tool, CEVICHE, was then used to compute numerical gradients of the objective with respect to the training parameters via forward-mode differentiation [23]. We then used the Adam optimization algorithm [25] (gradient ascent with momentum, in essence) to iteratively adjust  $\rho$  and thereby maximize  $\mathcal{L}$ . Optimization was conducted with learning rates ranging from 0.01 to 0.05 and the default Adam hyperparameters  $\beta_1 = 0.9$  and  $\beta_2 = 0.999$ .

The polarization of the input source has a strong effect in devices of this nature, either  $E_z$  ( $E$  out of the page), which we call the transverse magnetic (TM) polarization, or  $E_x$  ( $H$  out of the page), which we call the transverse electric (TE) polarization, with the latter case benefiting (and suffering, depending on the desired device functionality) from the presence of localized surface-plasmon (LSP) modes [26–29], while the former makes more direct use of dispersive and refractive effects [27,30,31]. In our previous studies [17,22], we see that for devices that seek to preserve an input signal like those we present here, the TE polarization leads to poor performance, so we choose to focus on the TM mode alone in this study. Thus, we will not expect to see any small sub-wavelength-scale field structures around our plasma elements or the large transmission losses that are indicative of the presence of LSP modes.

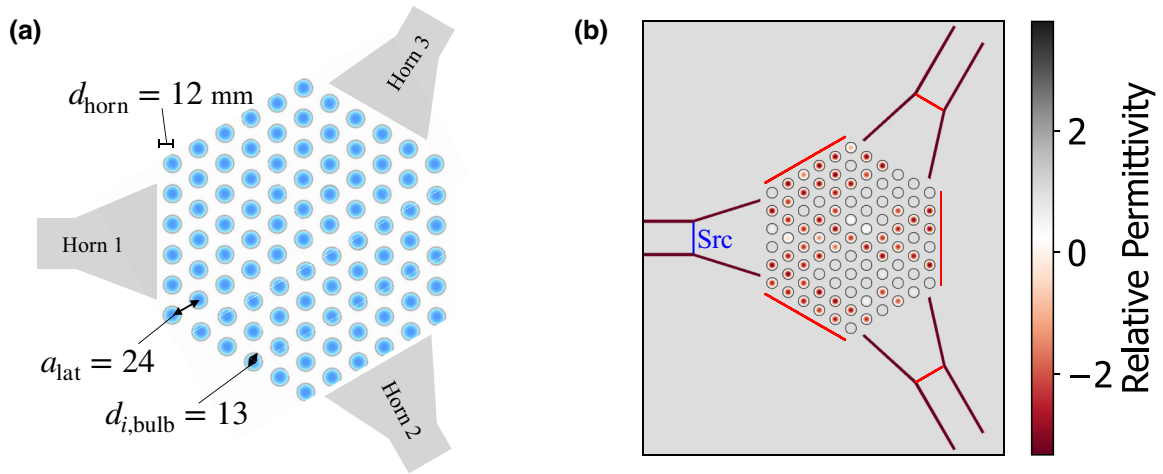


FIG. 3. A schematic of PMM (a) and the relative permittivity of the simulation domain (b), with the source (Src) and objective evaluation locations denoted in blue and red, respectively. The domain is shown with an arbitrary device configuration as an example.

To summarize, the PMM optimization problem can be expressed as

$$\begin{aligned} & \max_{\rho} \quad \mathcal{L}(\mathbf{E}) \\ \text{given} \quad & \nabla \times \frac{1}{\mu_0} \nabla \times \mathbf{E} - \omega^2 \varepsilon(\omega, \rho) \mathbf{E} = -i\omega \mathbf{J}, \end{aligned}$$

where  $\mathcal{L}$  is the objective, composed of a set of  $L_2$  inner-product integrals of the simulated field with the desired propagation mode,  $\mathbf{E}$  is the electric field,  $\rho$  is an  $n$ -dimensional vector (where  $n$  is the number of elements) that contains the parameters that set the plasma frequency of each of the PMM elements,  $\mu_0$  is the vacuum permeability,  $\omega$  is the field frequency,  $\varepsilon(\omega, \rho)$  is the spatially dependent permittivity that is encoded by  $\rho$ , and  $\mathbf{J}$  is a current density used to define a fundamental modal source at the input horn. In practice, the permittivity distribution among the plasma elements is controlled by varying the discharge current (which therein alters the plasma density) in each of the PMM elements according to the Drude model (discussed in Sec. I), which is where the dependence on  $\omega$  arises.

The beam-steering objective is the  $L_2$  inner product of the simulated field with an  $m = 1$  propagation mode (in order to preserve the input mode) evaluated at the probe in the desired exit minus the sum of the integrated field intensity at the incorrect exit and the other probe slices to discourage loss:

$$\mathcal{L}_{\text{steer}} = \int E \cdot E_{m=1}^* dl_{\text{desired exit}} - \sum_{\text{prb} \neq \text{desired exit}} \int |E|^2 dl_{\text{prb}}.$$

The optimization objective for the demultiplexer is quite different from the beam-steering case, since the objective

must take into account two separate simulations as the permittivity of the elements is frequency dependent. With this in mind, the demultiplexer objective is

$$\begin{aligned} \mathcal{L}_{mp} = & \left( \int E_{\omega_1} \cdot E_{m=1}^* dl_{\omega_1 \text{ exit}} \right) \left( \int E_{\omega_2} \cdot E_{m=1}^* dl_{\omega_2 \text{ exit}} \right) \\ & - \int |E_{\omega_1}|^2 dl_{\omega_2 \text{ exit}} - \int |E_{\omega_2}|^2 dl_{\omega_1 \text{ exit}} \\ & - \sum_{\text{prb} \neq \text{wvg exits}} \left[ \int |E_{\omega_1}|^2 dl_{\text{prb}} + \int |E_{\omega_2}|^2 dl_{\text{prb}} \right], \end{aligned}$$

where  $E_{\omega_1}$  is the simulated field for the first frequency and  $E_{\omega_2}$  is the simulated field for the second frequency. The first term in the objective is a product, so that it ensures that the fields reach the exit horn for both operating frequencies (therein avoiding local minima, where one gets good performance for just one of the two frequencies), the second two terms discourage leakage into the incorrect exits for each frequency, and the final term discourages leakage out of the device for both operating frequencies. For both objectives, each term is normalized by its value in the initial design iteration.

The maximum plasma frequency of the elements is set to be 8 GHz in the computational-optimization procedure, as that was our conservative estimate for the nominal maximum plasma density of our experimental sources. The optimal parameters from the computational inverse-design process are then used to set the configuration of the experimental device according to the mapping defined in Sec. II B.

## B. Experimental realization

The experimental plasma elements in this study are custom-manufactured UV germicidal discharge tubes



made of high-purity quartz ( $\epsilon = 3.8$ ), with an inner tube diameter of 13 mm and an outer diameter of 15 mm. The tubes are filled with argon gas at a fill pressure between 200 and 300 Pa, with a small amount of mercury present in each discharge to provide the UV radiation. The use of UV discharge tubes is necessary because other types of off-the-shelf discharge tubes (for lighting applications) often have a fluorescent coating applied to the glass that is opaque to microwave-range radiation. When operating, the tubes are estimated to have a gas temperature between 315 and 330 K according to infrared-thermometer measurements. The discharges are designed to operate with alternating current (ac) at a frequency between 20 and 50 kHz depending on the ballast circuit that is used. The nominal operating current and voltage are 24 V and 0.6 A, respectively, for a power of approximately 15 W. To push the discharges to higher plasma densities, we drive them with 24 W dc ballasts (Beasun RL15-425-18D24), each having its own dedicated programmable dc power supply (Longwei LW-3010). The dc power supplies are connected to a RS485 serial communication bus (with a maximum of 32 power supplies per RS485 bus) and accept MODBUS protocol serial commands from a custom PYTHON library via a USB-to-RS485 converter. A schematic and photograph of the experimental scheme are included in Fig. 4.

In practice, the discharges can be tuned through a fairly large range of plasma frequencies by setting the current of the dc power supply to its maximum value and then limiting the output voltage. The discharges typically operate from a maximum dc-power-supply voltage of 32 V down to about 6 V and then fail to maintain the discharge at a plasma frequency of about 2.4–4 GHz. We refer to this as the “voltage-tuning” mode. If the power supply is set to maximum voltage and the current is instead limited, a different operating mode can be reached, allowing us to access lower plasma-frequency values all the way down to 0.4 GHz before the discharge extinguishes. For the high-power ballasts used in this study, we achieve steady operation in the current tuning mode from approximately 60 mA to 200 mA.

In order to use the parameters from the *in silico* optimization that correspond to the plasma frequency of each of the plasma elements, we need to generate a mapping between the plasma frequency and the power-supply settings that produce that frequency. This is quite challenging, as we do not know the precise manufacturer fill pressure or gas temperature and the plasma density in our operating range is too small to use optical diagnostics for direct measurements. To combat this and obtain an approximate mapping from the power-supply settings to the

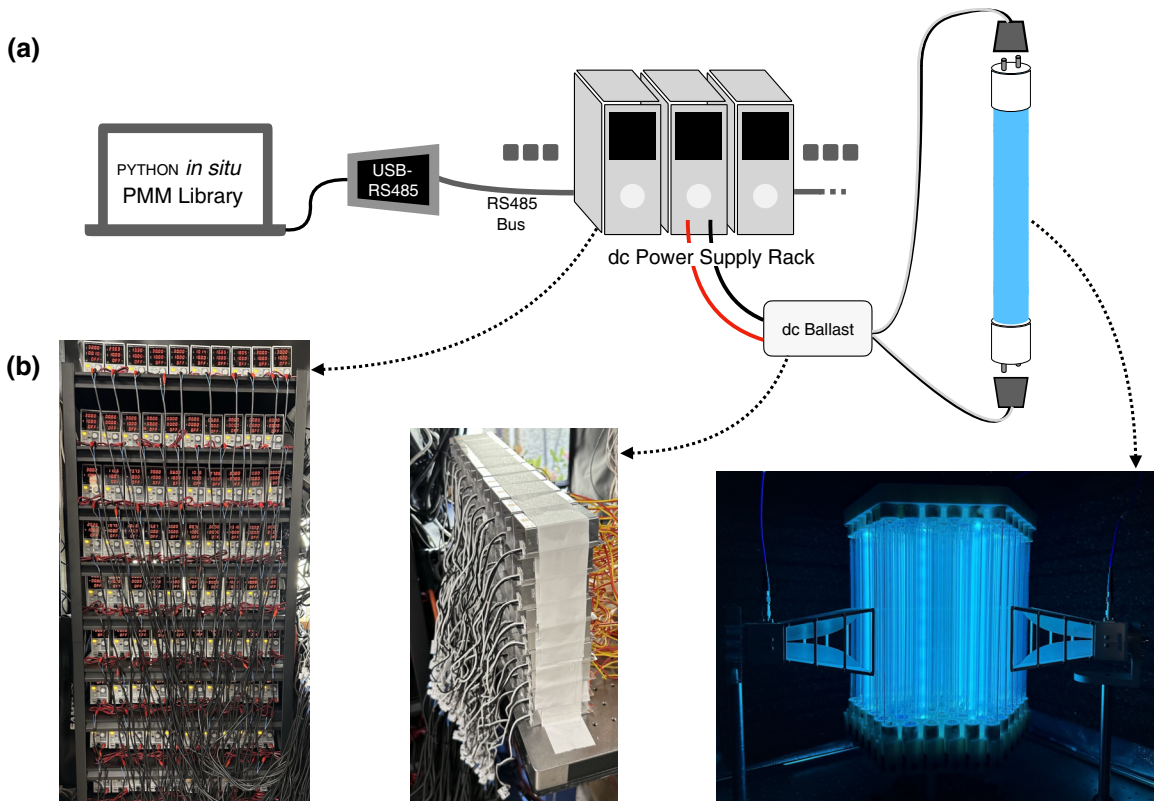


FIG. 4. A schematic of the experimental PMM system (a) and photographs of the different components of the apparatus (b), including the dc power supplies (left), the ballasts (middle), and the PMM itself, activated in an arbitrary configuration (right).

plasma frequency, we use a zero-dimensional kinetic simulation of the electron-energy distribution function (EEDF) within a plasma discharge, BOLSIG+ [32,33], assuming a known reduced electric field,  $E/n$ , where  $n$  is the estimated neutral-gas-number density. Our estimate for the neutral-gas-number density is obtained using the ideal-gas law along with estimates of the fill pressure and neutral-gas temperature. We measure the time-varying voltage across and current through the plasma discharge for a range of operating conditions. The rms voltage, estimated neutral-gas-number density, and estimates of the length of the discharge enable estimates of  $E/n$ . The EEDF determined using BOLSIG+ yields the electron mobility. The product of the mobility and the electric field provides the space-averaged electron drift velocity  $u_d = \mu_e E$  within the discharge. Finally, we can estimate the electron density using the measured current;  $n_e = I_{\text{rms}}/eu_d A_{\text{tube},i}$ , yielding the plasma frequency. Here,  $A_{\text{tube},i}$  is the internal cross-section area of the discharge tube. We note that this is a complex path to determine the plasma frequency, where several sources of uncertainty may be encountered.

Although the discharge frequency is much higher than the plasma recombination rate and, as such, the plasma density is quasisteady, we have confirmed, via high-speed photography, that at the peak of the voltage cycle, the plasma has the structure of a dc glow discharge, with

cathode and Faraday dark spaces clearly visible. At low-plasma-density operating conditions, we also observe striations in the positive column of the discharge. This means that when considering the effective electric field applied to the plasma that we feed to the BOLSIG+ kinetic model, we have to take into account the cathode fall voltage and be sure that we use the correct discharge length. For our discharges, the discharge length varies between 190 mm in the current-limited mode and 230 mm in the voltage-limited mode and we estimate the cathode fall voltage to be somewhere between 6 and 11 V [34]. Taking all of these considerations into account, we perform a sweep of all parameters (fill pressure, temperature, and cathode fall voltage) and perform a one-term polynomial fit that allows us to sweep between the highest- and lowest-density cases by varying a parameter  $k \in [0, 1]$ . Since the plasma-frequency values appeared to be slightly too large for these types of discharges (owing to the many uncertainties in determining plasma density), we have also added a scale factor  $S$  that would allow us to adjust the fit to lower values over the entire tuning range. The quasiexperimental fit is included in Fig. 5.

In addition to the high-speed-photography images mentioned above, we have also conducted Schottky-diode measurements of the transient dielectric response of the discharges as they are activated and deactivated, showing

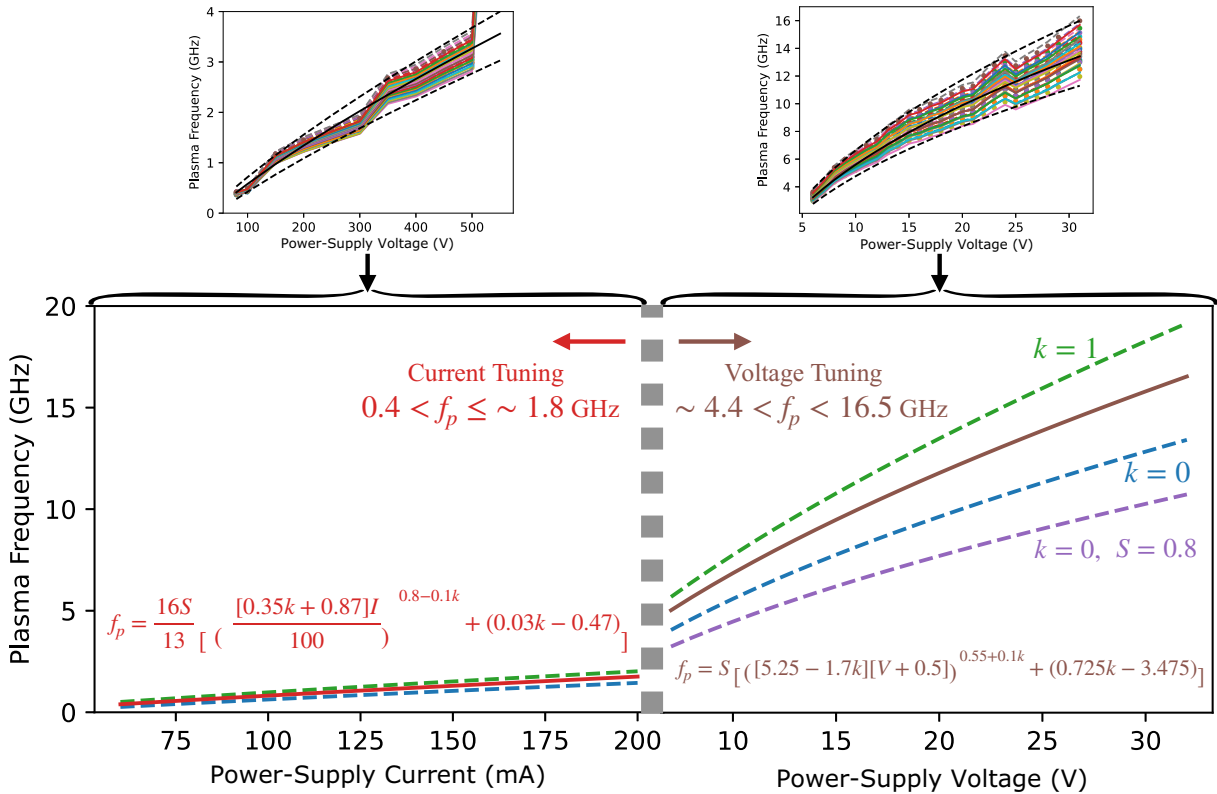


FIG. 5. The quasiexperimental mapping for plasma tuning (bottom) and the plots including all the cases from the parameter sweep in BOLSIG+ that form the basis for the mapping (top).

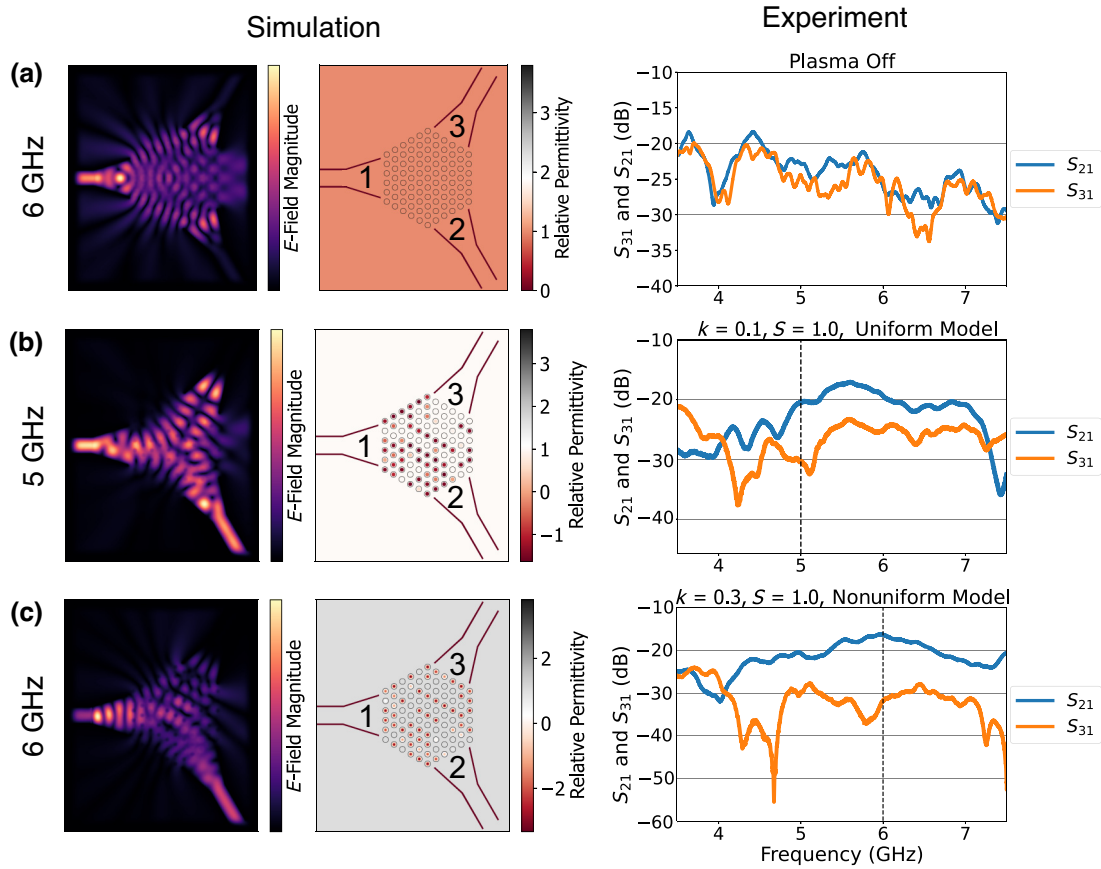


FIG. 6. Field simulations  $|\mathbf{E}_z|$  and optimal device domains  $\text{Re}[\varepsilon]$  (left) along with experimental transmission spectra (right) for (a) the PMM device with all the elements inactive, (b) the 5-GHz operating frequency optimal beam-steering design, and (c) the 6-GHz operating frequency optimal beam-steering design. The vertical dashed black lines indicate the design frequency in (b) and (c) and the fit parameters  $k$  and  $S$  are given along with the plasma-element model used (for details, see Sec. II).

that the rise time of the dielectric response is approximately 10 ms and the fall time is approximately 60 ms. Due to the current configuration of the device, where each RS485 bus hosts up to 25 power supplies, the actual time to set and activate the array is much longer, about 7 s, since each discharge is set and activated in series to avoid crosstalk within each RS485 bus. In practice, should a user need faster actuation, they need only parallelize the computational-array setting procedure and use more RS485 buses. The theoretical limit is to have one CPU process communicating directly with a single power supply at a time, with as many processes running in parallel as necessary. Since the power supplies operate at 9600 baud, each message is 8 bytes, and each actuation requires two messages (set voltage and current, and activate), the total time added by the communication protocol is about 15 ms, so the time to switch the entire array on could be lowered to approximately 25 ms and the deactivation time could be reduced to approximately 75 ms. Temporal modulation of the plasma frequency of an already-running discharge could occur at a maximum of about 75 Hz. Of course, more sophisticated communication protocols and

interconnects along with specially designed power supplies and ballast circuits could push these actuation times down further. Experimental data supporting these claims about the discharge structure and switching time can be found in the appendix of Ref. [35].

To perform the measurements described in Sec. III, we first construct the apparatus as pictured in Fig. 4, place the array into a custom-made anechoic chamber consisting of a box with microwave absorber panels attached to the interior surfaces, and then carry out an initial warm up of the device by turning every element in the device on for 15 s of every minute over a period of 10 min. This warm-up procedure makes sure that the temperature of the discharge tube will be steady throughout the measurements and it also allows the three-dimensionally- (3D) printed scaffolding to reach its steady operating temperature such that it will not flex and/or deform between measurements. Once the warm-up period is concluded, the PMM is activated according to the optimal parameters from the *in silico* optimization procedure for 15 s of each minute for as many minutes as it takes for all measurements to be collected. As stated before, the PMM device can activate and set

the operating conditions for 91 elements in about 7 s. PYTHON scripts are constructed to ensure that the PMM is not allowed to cool to room temperature by failing to maintain the 15 s/min duty cycle.

For each measurement,  $S_{21}$  and  $S_{31}$  are measured by a Rohde and Schwarz ZNB40 4-port vector network analyzer that has been calibrated using a Rohde and Schwarz ZN-Z54 calibration unit. The  $S$  parameters are collected in 10 000 points from 2 to 12 GHz, with an averaging factor of 10. For each device objective, we test the optimal parameters for three different plasma-element models (uniform-density profile, Bessel-function profile, and Bessel-function profile with collisions (for more details regarding the plasma model, see Ref. [22]) and sweep the fitting parameters  $k$  and  $S$  to attempt to find the correct plasma-frequency mapping. This corresponds to about 30 measurements for each objective and the best or most informative case is displayed in Sec. III.

### III. RESULTS

#### A. Beam steering

The simulated and experimental results for the beam-steering objective where a source delivers power to one of two receiving ports are presented in Fig. 6. During

the *in silico* optimization, the plasma density within each discharge is modeled as being either uniform with no collisions, nonuniform with no collisions, or nonuniform with collisions with  $k$  and  $S$  used to parametrize the relationship between the plasma density and operating voltage or current (see Fig. 5).

As expected, when all elements are inactive [Fig. 6(a)] the spectra of both ports are nearly identical within about 5 dB of one another at all frequencies. The small differences between the two measured spectra [right frame in Fig. 6(a)] are due to minor defects in the device scaffold and in the alignment of the microwave horns. In both the 5- and 6-GHz active configurations, the transmission in port 2 (the desired port) is nearly maximal at the frequency for which the device was optimized and we have about (10–15)-dB isolation between the ports. In the 5-GHz configuration in particular, there is a drop in transmission in port 3 at almost precisely the operating frequency predicted by the simulations assuming a uniform plasma model with a discharge-voltage mapping to plasma density defined by  $k = 0.1$  and  $S = 1.0$ . In the 6-GHz plasma active case we see even better isolation at another frequency point, with over 30-dB isolation at about 4.7 GHz with a transmission in port 2 almost as high as at the operating frequency. We discuss the possible cause(s) for this and its

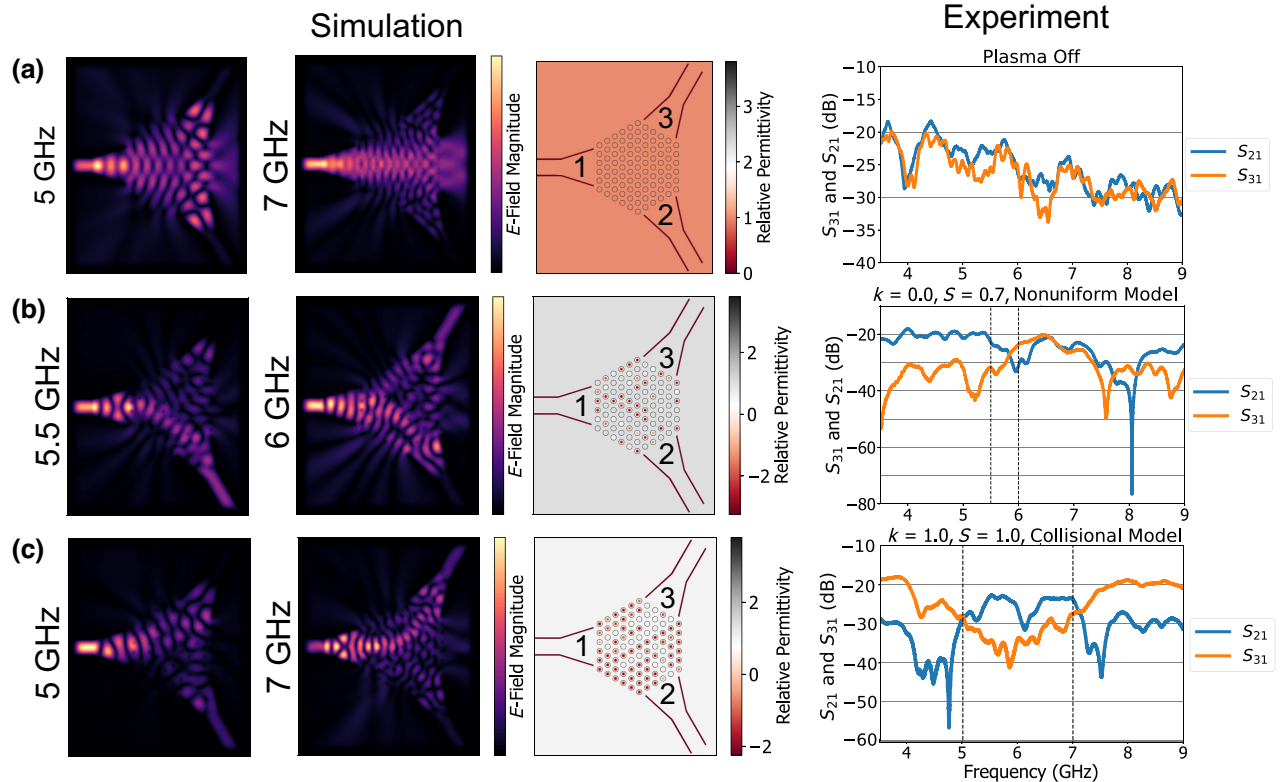


FIG. 7. Field simulations  $|\mathbf{E}_z|$  and optimal device domains  $\text{Re}[\varepsilon]$  (left) along with experimental transmission spectra (right) for (a) the PMM device with all the elements inactive at 5 and 7 GHz, (b) the 5.5- or 6-GHz optimal demultiplexer design and, (c) the 5- or 7-GHz optimal demultiplexer design. The vertical dashed black lines indicate the design frequencies in (b),(c), and the fit parameters  $k$  and  $S$  are given along with the plasma-element model used (for details, see Sec. II).



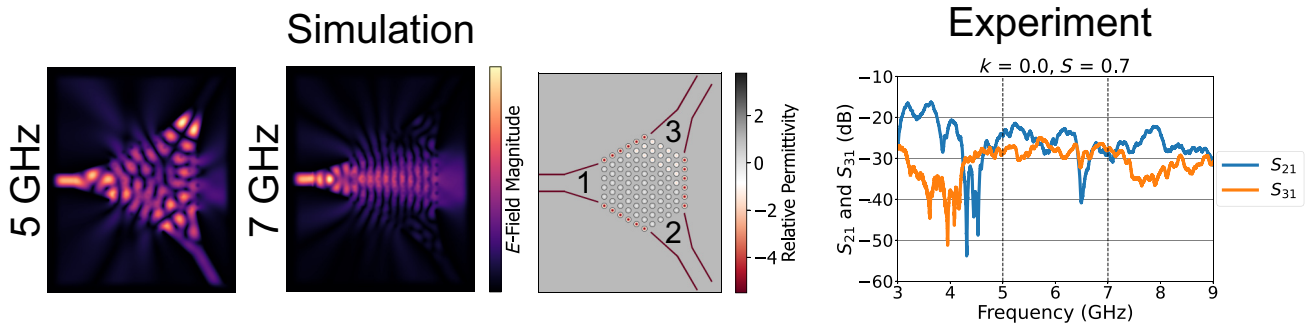


FIG. 8. Field simulations  $|\mathbf{E}_z|$  and optimal device domains  $\text{Re}[\varepsilon]$  (left) along with experimental transmission spectra (right) for the PMM device, with our best attempt at an *a priori* human-designed 5- or 7-GHz demultiplexer. The vertical dashed black lines indicate the design frequencies and the fit parameters  $k$  and  $S$  are chosen according to the best values for the devices conceived via inverse design.

significance in Sec. IV. In both cases, the power-supply setting to plasma-density fitting parameters that led to the best performance ( $k \approx 0.2$  and  $S = 1.0$ ), suggest that the actual maximum plasma density of the discharges when driven by their power supplies is about 14 GHz (for details, see Fig. 5) although prolonged operation at this power level causes damage to the discharge.

### B. Demultiplexer

The simulated and experimental results for the demultiplexer objective are presented below in Fig. 7. Here, we use the same device as that above, but seek to separate different source frequencies. For example, in Fig. 7(b), we direct 5.5- and 6-GHz content sourced at port 1, to ports 2 and 3, respectively.

Figure 7(a) shows the baseline inactive plasma case, with experiments once again indicating that ports 2 and 3 receive similar signals (within 3–5 dB) over a wide range of frequencies. With active plasma cases, we find the best performance for the nonuniform model using  $k = 0.0$  and  $S = 0.7$  (similar to the beam-steering objective) for the 5.5- or 6-GHz demultiplexer [Fig. 7(b)], but for the 5- or 7-GHz demultiplexer [Fig. 7(c)] we see the transmission characteristics that we want for the collisional plasma-element model at  $k = 1.0$  and  $S = 1.0$ . In the 5.5- or 6-GHz case, the transmission spectrum appears as one would expect in the region of the operating frequencies, with the transmission of the two ports crossing at the midpoint between the operating frequencies, where we see about 10-dB isolation in the correct direction. Interestingly, the same configuration performs the demultiplexer objective at the frequencies of approximately 5.25 GHz and 8.05 GHz with up to 40-dB isolation, hinting at the potential of the device if the optimization was to be carried out *in situ*. The 5- or 7-GHz demultiplexer does not perform its objective properly at the design frequencies but, instead, performs very well at the slightly shifted frequencies of about 5.6 and 7.4 GHz.

In Fig. 8, we see the simulated and experimental results when a 5- or 7-GHz demultiplexer is designed by hand by creating what would function as low-index bridges to the correct output port for either design frequency. The general principle is that port 3 is protected by a region of sources that have an average plasma frequency of approximately 6 GHz, so that those elements serve as a reflective barrier to the 5-GHz source but are transparent to the 7-GHz source. The edges of the domain are set to their maximum plasma density to discourage leakage.  $k = 0.0$  and  $S = 0.7$  were chosen as the fitting parameters to limit the voltage of the edge elements and avoid damaging the discharges. In both the simulation and the experiment, the device does not appear to steer the 7-GHz source to either output and there is only slight isolation between the ports in the correct direction at 5 GHz. The experimental spectrum is fairly unremarkable, without obviously meaningful structures at any frequency.

## IV. DISCUSSION AND CONCLUSIONS

The results presented in Sec. III show that although we can reliably get somewhat strong performance by optimizing our devices *in silico*, there are ultimately some shortcomings. In most cases, the configurations actually resulted in better performance at frequencies other than the design frequency, as seen with the 6-GHz beam-steering device in Fig. 6 and the 5.5- or 6-GHz demultiplexer in Fig. 7. These cases show that up to approximately 40-dB isolation is achievable in practice at various frequencies throughout the frequency domain, indicating that the device has a high degree of dynamic range (possibly due to some manner of Fabry-Perot resonance effect), but the *in silico* optimizer was only able to produce (10–15)-dB isolation at the design frequencies.

While there can be a few reasons for these shortcomings, we attribute them to simplifications made in the simulations. The *in silico* optimization procedure uses a 2D domain with plasma elements of varying levels of

complexity. The most sophisticated plasma-element model that includes both a nonuniform plasma-density profile and collisional damping failed to produce the best performance in all but one case, illustrating that we still lack the detailed knowledge of the discharge properties that are needed to produce robust results at design conditions. Furthermore, the system is not entirely electromagnetically isolated as assumed in the simulations. To avoid interference due to scattering from the surroundings of the PMM, the experiments are carried out in a custom-fabricated anechoic chamber but even this is not entirely sufficient. In addition, the finite size of the tubes brings the electrodes and the wiring into play, both of which undoubtedly interact with the source fields. Unfortunately, a 3D simulation that takes many of these nonideal conditions into account is far too costly to use within an inverse-design scheme.

We also found that the mapping between the power-supply settings (voltage or current) and the plasma frequency of the discharge tubes, facilitated by the electron-energy distribution solver, BOLSIG+, tends to overestimate the plasma density, where only the lowest-density case according to the BOLSIG+ calculations is compatible with the experimental results ( $k = 0$ ). One interesting departure from the other results regarding the experimental mapping is that the 5- or 7-GHz demultiplexer performs best for the collisional plasma-element model at  $k = 1.0$  and  $S = 1.0$ , indicating that when using that element model, the optimal plasma frequencies from the *in silico* optimization are necessarily larger. Because the elements are lossy, the optimizer may be biased to higher plasma densities to encourage scattering off the plasma elements instead of propagation through them. It is also possible that the collisionality is stronger in the experimental device at higher power (the collision frequency is assumed to be 1 GHz in the *in silico* collisional plasma model); therefore, to match the simulated result, one has to decrease the plasma frequency in the experiment. Also, since the device does not function at precisely the intended frequencies, it is possible that this configuration was simply stumbled upon by chance. Many of these challenges can be avoided by *in situ* optimization.

The attempt at designing the device intuitively for objectives such as the demultiplexer is an illustration of how we cannot hope to outperform inverse design, particularly so when our model of the physical device is not precise. Despite the shortcomings discussed above, the devices still show strong evidence that the *in silico* optimization can result in performance that at least addresses the design criteria, if not with a high degree of efficiency. Designing by intuition is therefore not an option; but, of course, we have also shown here that the *in silico* inverse-design procedure fails to fully utilize the dynamic range of the system elements. Luckily, since our device is composed entirely of plasma elements, we can perform the inverse-design process entirely *in situ*.

Fully *in situ* inverse design addresses almost all the shortcomings described above and also opens up many exciting opportunities. We no longer have to be concerned with the fidelity of the modeling, since we will be using the physical device to perform the optimization. Since we find that the device is capable of approximately 50-dB isolation at various frequencies, we would expect to be able to achieve this and likely more, since those cases were obtained accidentally. This also presents an opportunity to refine our element model. Once a high-performance design is achieved via *in situ* inverse design, the parameters can be fed into a simulation domain where we modify the plasma model until we see the same performance, allowing us to more thoroughly understand the physics of our plasma sources. Moving to fully *in situ* optimization also removes some of the limitations on our geometry. As mentioned before, 3D geometry would be far too computationally costly to use for *in silico* inverse design but it incurs no extra cost in *in situ* inverse design. Thus, we could use device structures such as that of Ref. [27]. Even for this 2D configuration, each iteration in the optimization procedure can take 10 min with a 64-core workstation, while the *in situ* iterations can be limited to mere seconds in practice, regardless of the geometry. We have also shown in prior work that our plasma sources have a pronounced gyrotropic response when magnetized [36,37] but materials with anisotropic permittivity tensors, such as magnetized plasma, cannot be modeled with our simulation tool. By using a large Helmholtz configuration, entire PMM devices can be magnetized to take advantage of the very rich physics inherent in magnetized plasmas.

In conclusion, we show in this study that PMM devices can be optimized *in silico* to perform beam steering and demultiplexing at a level of performance that is not possible to obtain using conventional intuitive design methods. Ultimately, the *in silico* inverse-design process has shortcomings that lead to a failure to utilize the full potential of the PMM configuration. Since the PMM device can be reconfigured in seconds or less, the inverse-design process can be performed entirely *in situ*, side-stepping the computational cost and modeling inaccuracies associated with *in silico* inverse design, thereby promising better performance.

## ACKNOWLEDGMENTS

We would like to thank Dr. Benjamin Wang for his assistance in procuring the experimental components for this study. This research is supported by the Air Force Office of Scientific Research through a Multi-University Research Initiative (MURI), Grant No. FA9550-21-1-0244, with Dr. Mitat Birkan and Dr. Arje Nachman as the Program Managers. J.A.R. acknowledges support from the Charles H. Kruger Stanford Graduate Fellowship.

- [1] L. Su, D. Vercruysee, J. Skarda, N. V. Sapra, J. A. Petykiewicz, and J. Vučković, Nanophotonic inverse design with SPINS: Software architecture and practical considerations, *Appl. Phys. Rev.* **7**, 11407 (2020).
- [2] O. D. Miller, Photonic design: From fundamental solar cell physics to computational inverse design, arXiv preprint [ArXiv:1308.0212](https://arxiv.org/abs/1308.0212) (2013).
- [3] D. Liu, L. H. Gabrielli, M. Lipson, and S. G. Johnson, Transformation inverse design, *Opt. Express* **21**, 14223 (2013).
- [4] T. W. Hughes, M. Minkov, I. A. Williamson, and S. Fan, Adjoint method and inverse design for nonlinear nanophotonic devices, *ACS Photon.* **5**, 4781 (2018).
- [5] S. Molesky, Z. Lin, A. Y. Piggott, W. Jin, J. Vucković, and A. W. Rodriguez, Inverse design in nanophotonics, *Nat. Photon.* **12**, 659 (2018).
- [6] R. E. Christiansen and O. Sigmund, Inverse design in photonics by topology optimization: Tutorial, *JOSA B* **38**, 496 (2021).
- [7] N. M. Andrade, S. Hooten, S. A. Fortuna, K. Han, E. Yablonovitch, and M. C. Wu, Inverse design optimization for efficient coupling of an electrically injected optical antenna-led to a single-mode waveguide, *Opt. Express* **27**, 19802 (2019).
- [8] R. E. Christiansen, Z. Lin, C. Roques-Carnes, Y. Salamin, S. E. Kooi, J. D. Joannopoulos, M. Soljačić, and S. G. Johnson, Fullwave Maxwell inverse design of axisymmetric, tunable, and multi-scale multi-wavelength metalenses, *Opt. Express* **28**, 33854 (2020).
- [9] M. Meem, S. Banerji, C. Pies, T. Oberbiermann, A. Majumder, B. Sensale-Rodriguez, and R. Menon, Large-area, high-numerical-aperture multi-level diffractive lens via inverse design, *Optica* **7**, 252 (2020).
- [10] R. Pestourie, C. Pérez-Arancibia, Z. Lin, W. Shin, F. Capasso, and S. G. Johnson, Inverse design of large-area metasurfaces, *Opt. Express* **26**, 33732 (2018).
- [11] H. Chung and O. D. Miller, Tunable metasurface inverse design for 80% switching efficiencies and 144° angular deflection, *ACS Photon.* **7**, 2236 (2020).
- [12] P. I. Borel, A. Harpoth, L. H. Frandsen, M. Kristensen, P. Shi, J. S. Jensen, and O. Sigmund, Topology optimization and fabrication of photonic crystal structures, *Opt. Express* **12**, 1996 (2004).
- [13] M. Minkov, I. A. Williamson, L. C. Andreani, D. Gerace, B. Lou, A. Y. Song, T. W. Hughes, and S. Fan, Inverse design of photonic crystals through automatic differentiation, *ACS Photon.* **7**, 1729 (2020).
- [14] M. Burger, S. J. Osher, and E. Yablonovitch, Inverse problem techniques for the design of photonic crystals, *IEICE Trans. Electron.* **87**, 258 (2004).
- [15] Z. Lin, A. Pick, M. Lončar, and A. W. Rodriguez, Enhanced spontaneous emission at third-order Dirac exceptional points in inverse-designed photonic crystals, *Phys. Rev. Lett.* **117**, 107402 (2016).
- [16] J. Jiang, M.-K. Chen, and J. A. Fan, Deep neural networks for the evaluation and design of photonic devices, *Nat. Rev. Mat.* **6**, 679 (2020).
- [17] J. A. Rodríguez, A. I. Abdalla, B. Wang, B. Lou, S. Fan, and M. A. Cappelli, Inverse design of plasma metamaterial devices for optical computing, *Phys. Rev. Appl.* **16**, 014023 (2021).
- [18] V. Nikkhah, A. Pirmoradi, F. Ashtiani, B. Edwards, F. Afla-touni, and N. Engheta, Inverse-designed low-index-contrast structures on silicon photonics platform for vector-matrix multiplication (2023), [ArXiv:2302.00793](https://arxiv.org/abs/2302.00793).
- [19] A. Y. Piggott, J. Lu, K. G. Lagoudakis, J. Petykiewicz, T. M. Babinec, and J. Vučković, Inverse design and demonstration of a compact and broadband on-chip wavelength demultiplexer, *Nat. Photon.* **9**, 374 (2015).
- [20] L. Su, A. Y. Piggott, N. V. Sapra, J. Petykiewicz, and J. Vuckovic, Inverse design and demonstration of a compact on-chip narrowband three-channel wavelength demultiplexer, *ACS Photon.* **5**, 301 (2018).
- [21] Q. Huang, L. T. Gan, and J. A. Fan, Conformal volumetric grayscale metamaterials, *Adv. Mater.* **35**, 2204688 (2023).
- [22] J. A. Rodríguez and M. A. Cappelli, Inverse design of plasma metamaterial devices with realistic elements, *J. Phys. D: Appl. Phys.* **55**, 465203 (2022).
- [23] T. W. Hughes, I. A. D. Williamson, M. Minkov, and S. Fan, Forward-mode differentiation of Maxwell's equations, *ACS Photon.* **6**, 3010 (2019).
- [24] S. Pai, Z. Sun, T. W. Hughes, T. Park, B. Bartlett, I. A. D. Williamson, M. Minkov, M. Milanizadeh, N. Abebe, F. Morichetti, A. Melloni, S. Fan, O. Solgaard, and D. A. B. Miller, Experimentally realized in situ backpropagation for deep learning in photonic neural networks, *Science* **380**, 398 (2023).
- [25] D. P. Kingma and J. Ba, Adam: A method for stochastic optimization (2014), [ArXiv:1412.6980](https://arxiv.org/abs/1412.6980).
- [26] F. Righetti, B. Wang, and M. Cappelli, Enhanced attenuation due to lattice resonances in a two-dimensional plasma photonic crystal, *Phys. Plasmas* **25**, 124502 (2018).
- [27] B. Wang, J. A. Rodríguez, and M. A. Cappelli, 3D woodpile structure tunable plasma photonic crystal, *Plasma Sources Sci. Technol.* **28**, 02LT01 (2019).
- [28] O. Sakai, A. Iwai, Y. Omura, S. Iio, and T. Naito, Wave propagation in and around negative-dielectric-constant discharge plasma, *Phys. Plasmas* **25**, 031901 (2018).
- [29] O. Sakai, J. Maeda, T. Shimomura, and K. Urabe, Functional composites of plasmas and metamaterials: Flexible waveguides, and variable attenuators with controllable phase shift, *Phys. Plasmas* **20**, 073506 (2013).
- [30] B. Wang and M. A. Cappelli, Waveguiding and bending modes in a plasma photonic crystal bandgap device, *AIP Adv.* **6**, 65015 (2016).
- [31] B. Wang and M. A. Cappelli, A plasma photonic crystal bandgap device, *Appl. Phys. Lett.* **108**, 161101 (2016).
- [32] G. J. M. Hagelaar and L. C. Pitchford, Solving the Boltzmann equation to obtain electron transport coefficients and rate coefficients for fluid models, *Plasma Sources Sci. Technol.* **14**, 722 (2005).
- [33] SIGLO database
- [34] A. Hilscher, Determination of the cathode fall voltage in fluorescent lamps by measurement of the operating voltage, *J. Phys. D: Appl. Phys.* **35**, 1707 (2002).
- [35] J. A. Rodríguez, Ph.D. thesis, Stanford University, School of Engineering (2023).

- [36] L. S. Houriez, H. Mehrpour Bernety, J. A. Rodríguez, B. Wang, and M. A. Cappelli, Experimental study of electromagnetic wave scattering from a gyrotropic gaseous plasma column, *Appl. Phys. Lett.* **120**, 223101 (2022).
- [37] H. M. Bernety, L. S. Houriez, J. A. Rodríguez, B. Wang, and M. A. Cappelli, A characterization of plasma properties of a heterogeneous magnetized low pressure discharge column, *AIP Adv.* **12**, 115220 (2022).